



# Strain sensing based on resonant states in 2D dielectric photonic quasicrystals

ANGEL ANDUEZA,<sup>1,2,\*</sup>  JESÚS PÉREZ-CONDE,<sup>3,4</sup> AND JOAQUÍN SEVILLA<sup>1,2</sup>

<sup>1</sup>Dpto. Ing. Eléctrica, Electrónica y de Comunicación, Universidad Pública de Navarra, 31006 Pamplona, Spain

<sup>2</sup>Smart Cities Institute (SCI), Universidad Pública de Navarra, 31006 Pamplona, Spain

<sup>3</sup>Dpto. de Ciencias, Universidad Pública de Navarra, 31006 Pamplona, Spain

<sup>4</sup>Institute for Advanced Materials (INAMAT), Universidad Pública de Navarra, 31006 Pamplona, Spain

\*angel.andueza@unavarra.es

**Abstract:** This paper reports the numerical and experimental study of the strain sensing effect of bidimensional quasiperiodic structures made with dielectric cylinders. Structures of around 100 cylinders arranged following a Penrose quasiperiodic disposition were simulated, built and measured, in different states of deformation. The selected quasiperiodic structure contains a symmetric decagonal ring resonator that shows two states in its photonic band gap. The frequency of these states varies linearly in opposite directions as the structure is axially deformed, becoming an interesting sensing principle that can be exploited to build optical strain gauges. As a proof of concept, centimeter-scale glass cylinder ( $\epsilon_r=4.5$ ) structures were fabricated and their transmission spectra were measured in the microwave range. The same structures were simulated using finite integration time domain showing a good agreement with the measurements. The sensitivity of the prototype built was 12.4 kHz/ $\mu\epsilon$ , very linear in a wide range. Therefore, we conclude that the states in the gap of the resonator rings of 2D quasicrystals can find an interesting application in optical strain gauge construction.

© 2021 Optical Society of America under the terms of the [OSA Open Access Publishing Agreement](#)

## 1. Introduction

Nowadays, there are a high number of industrial and civil engineering applications of practical interest in which sensing strain induced changes are important. In many fields, the real-time measurement of strain forces suffered by the components which are part of complex structures such as aircrafts, wind turbines, ships or buildings represents a significant engineering challenge.

Photonic crystals (PhCs) [1,2] are materials which present variation of the dielectric constant over distances of the same order of incident wavelength. Their spectral properties are highly dependent on construction details such as structure, dielectric permittivity and size. For that reason, it is possible to use PhC as sensors by making some of their structural characteristics responsive to the desired measurand. In the last two decades, the development of PhCs sensors has experienced a substantial increase due to their performance and to the increasing demand of sensing applications such as instrumentation, healthcare or industrial control. Mechanical sensing effects of PhC-based structures were also reported so far. In this context, PhCs represent a sophisticated solution for achieving high performance in strain sensing applications. In the literature it has been proposed diverse approximations to design a strain sensor based on PhCs structures. During the last decades, hundreds of papers have explored the possibility of employing PhCs as strain sensors. We distinguish three types of strain PhCs sensors depending on how spatial variation of the dielectric permittivity is distributed over the three orthogonal directions of the space: one (1D), two (2D) and three-dimensional strain PhCs sensors. 1D-PhCs based on Fiber Bragg Gratings (FBG) [3,4] and Long Period FBG [5,6] have been extensively proposed and implemented for stress measuring. These days, new sensors have been proposed as 1D strain

sensor by using Graphene Fibonacci (GF) PhCs [7] or nanorods [8]. Many other proposals have been published based on 2D PhCs cavities (PCC) [9]. These sensors are formed by introducing point defects in the orderly arranged lattices. Different proposals can be found in the literature for stress measure, some examples of this could be point defect cavities [10,11], slot cavities [12,13], ring cavities [14–16] and coupled-cavities [17]. Another example of 2D PhCs strain sensors that we can find is Photonic Crystal Fibers (PCFs), typically based on Sagnac [18] and Mach-Zender [19,20] Interferometers. Finally, 3D PhCs sensors of opal films [21–23] have been also reported for applications as stretch-tunable photonic band gap materials.

In this paper, we present a novel sensing principle based on the photonic properties of a structure created from a selected section of a 2D Penrose Quasiperiodic (QP) photonic crystal [24] built with dielectric cylinders. The sensing structure contains a collective ring resonator (CRR) [25] and a set of cylinders in an apparently disordered disposition. This structure presents a photonic gap with two states in it that are due to the resonances of the CRR. The stretching or compression of the structure deforms the CRR and produce an independent shift of the resonances in the transmission spectrum. The difference between the frequency values of the resonances can be therefore exploited to measure the deformation and, consequently, to the applied strain.

Numerical results, obtained by Finite Integrated Method (FIM), showed a differential shift linearly dependent on the applied strain (linearity error lower than 2.5%), of around 0.18 MHz per  $\mu\epsilon$ . A prototype of this sensor was built with glass cylinders and their microwave transmission spectra were measured for different deformation states. The agreement between measurement and numerical calculation is very good. We, therefore, conclude that the frequency shift of the two modes could be used to design a sensor where the strain of the structure would be determined by the difference of the transmission intensity between them.

Photonic quasicrystals present a highly isotropic bandgap, therefore the transmission intensity contrast between the two states and the background will be independent of the incidence angle therefore avoiding alignment mismatches. Besides, the coupling of free space radiation to the crystal has proven to be quite good, making unnecessary specifically designed waveguiding systems to feed the sensor prototype. Finally, the existence of two states allows to build a differential sensing procedure, with all the advantages of noise and cross-sensitivities reduction that it generates. All these characteristics make the sensing platform here presented a good competitor among the abovementioned ones.

## 2. Experimental

### 2.1. Sensor prototype design

It is well established [24–26] that quasicrystal dielectric structures present collective resonator rings responsible of states in the photonic gap of the structure. We aimed to check how the states evolve with the deformation of the structure. For practical purposes, the quasicrystal must be substituted by an approximant that retains the same structure order at local scale as the original quasicrystal but in a finite size. In our case, we started with a Penrose tiling of decagonal symmetry generated by tiles of edge length  $a$  and calculated an approximant of 243 vertices as described by Wang [24]. Cylinders of infinite length and radius  $r$  are placed perpendicular to the tiling plane in its vertices as shown in Fig. 1.

The length of the structure in the direction of the incoming radiation ( $W$  in Fig. 1) was then adjusted to obtain a maximum contrast between the states and the gap signals.

As exposed in a previous work [26], if  $W$  is too large radiation extinction in the gap is big enough to make undetectable the output signal. On the other hand, in too thin samples, all radiation bridges the structure shadowing individual state's signals. The width of the sample must be selected taking into account a compromise between the number of cylinders necessary to create the gap and the presence of, at least, a decagonal ring capable of exciting localized states in the gap. Therefore, we have chosen a value of the thickness of 1.2 times the higher

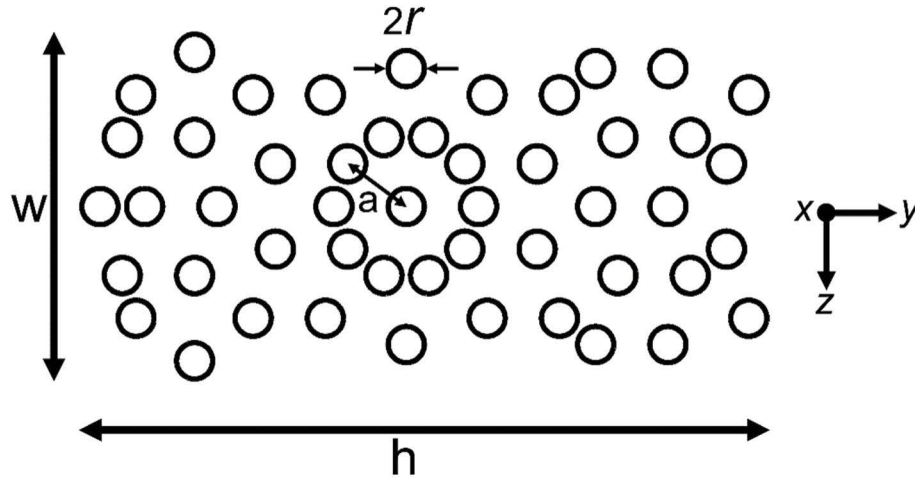


**Fig. 1.** Strain sensor design unit cell. Disposition of 49 glass cylinders that conforms the unit cell along y-axis. The cylinders present an infinite length in x-direction. The radius of the cylinders is  $r$  and  $a$  corresponds to the edge length of the quasicrystal photonic crystal. The sensor width is finite and its value is  $W$ . Radiation propagates in  $z$ -direction.

wavelength, which satisfies both premises and guarantees an electromagnetic response adequate for the purpose of this work.

The proposed prototype can be seen in Fig. 1. The narrowing of the initial approximant generates a photonic crystal device composed of only 49 cylinders of infinite length ( $x$ -direction) and including a spatial pitch  $h$  of  $(\tau^3 \cdot \sqrt{5}) \cdot a$  in the  $y$ -direction, with  $\tau$  the golden number  $\tau = (1 + \sqrt{5})/2$ . The thickness  $W$  of the lattice in the direction of the incoming field ( $z$ -direction) is finite and corresponds to 56 mm (1.2 times the higher wavelength of analysis).

## 2.2. Deformation of the structure

In order to investigate the structure's behavior when the symmetry of the lattice is broken by the effect of shear, we calculate the prototype deformation. Then, with a set of samples of well-defined deformation, we will calculate and measure their transmission spectra so that the position of the states in the gap can be followed.

A generic strain or deformation,  $\mathbf{D}$ , in two dimensions can be implemented with a deformation applied to every  $(z, y)$  point, so that the new transformed point  $(z', y')$  is written as,

$$\begin{pmatrix} z' \\ y' \end{pmatrix} = \mathbf{D} \cdot \begin{pmatrix} z \\ y \end{pmatrix} = \begin{pmatrix} a & b \\ c & d \end{pmatrix} \cdot \begin{pmatrix} z \\ y \end{pmatrix} = \begin{pmatrix} az + by \\ cz + dy \end{pmatrix}, \quad (1)$$

In addition, any deformation can be decomposed in a dilatation, a rotation and a shear of the lattice. We are interested in deformations that change the transmission spectrum of the lattice. Although global dilatations do produce a global shift of the whole spectra, this behavior can be also seen as a scaling of the lengths and frequencies in the Maxwell equations and no symmetry change is implied. Therefore, we restrict the possible deformation to pure shear which breaks the rotational  $n$ -fold symmetry of the structure and can be described by the matrix  $\mathbf{S}$ ,

$$\mathbf{S} = \begin{pmatrix} 1 & \gamma_z \\ \gamma_y & 1 \end{pmatrix}. \quad (2)$$

with  $\gamma_z$  and  $\gamma_y$  two real numbers which reflect the amount of the shear in the  $z$  and  $y$  directions, respectively. Negative values in shear parameters correspond to contraction or approximation between the cylinders, and positive values to expansion or distancing among them. As we only study shear in  $y$  direction, we will consider  $\gamma_z$  equal to zero and  $\gamma_y$  will be named as  $\gamma$  from this point on. Taking into account the previous simplification, the transformed points ( $z'$ ,  $y'$ ) from ( $z$ ,  $y$ ) are given from the matrix,

$$\begin{pmatrix} z' \\ y' \end{pmatrix} = \begin{pmatrix} 1 & 0 \\ \gamma & 1 \end{pmatrix} \cdot \begin{pmatrix} z \\ y \end{pmatrix} = \begin{pmatrix} z \\ y + z\gamma \end{pmatrix}. \quad (3)$$

An equivalent strain magnitude can be calculated from transformed coordinates after sheared the structure. Strain induced ( $\epsilon$ ) is the ratio of the change in position of the cylinder to the original, unaffected position, normalized by the unit of length. From Eq. (3), the amount of induced strain ( $\epsilon$ ) may be obtained in  $y$  directions as,

$$\epsilon_y = \frac{(y' - y)}{y} \cdot \gamma = \frac{z}{y} \cdot \gamma. \quad (4)$$

where  $y$  and  $z$  are the original coordinates of the cylinder and  $\gamma$  is the shear value applied in  $y$  direction. Although dimensionless, the strain is expressed in [m/m] or  $\epsilon$ . In practice, the magnitude of measured strain is very small, so it is often expressed as microstrain ( $\mu\epsilon$ ), which corresponds to  $\epsilon \times 10^{-6}$  m/m. Therefore, we can characterize a state of deformation by the  $\gamma$  value. To analyze the influence of shear (strain) into the electromagnetic response of the structure we study the transmission of samples with different deformations. In the same way that strain gauges work, we study the shear by applying only expansion deformation in one direction simultaneously. In the prototype previously described, to avoid cylinder collisions, the interval of  $y$  coordinate is  $\pm 7.65$  mm and the shear parameter  $\gamma$  ranges from 0 to 0.3. From Eq. (4), we can calculate the corresponding strain ranges, which vary from 0 to 65387  $\mu\epsilon$ . These values are well above the typical range of use of most strain gages in electronic instrumentation applications.

### 2.3. Sensor prototype construction

An experimental prototype of the sensor was fabricated using soda-lime glass cylinders with a dielectric permittivity at microwave frequencies of  $\epsilon_r = 4.5$ , radius  $r = 3$  mm and length  $L = 250$  mm (Fig. 2). The prototype is composed of 89 cylinders (40 more than unit cell shown in Fig. 1) and includes in the center a decagonal ring with 10-fold rotational symmetry as it appears in 2D Penrose tiling quasicrystals taken as a starting point. The reason to increment the number of cylinders of the sample is to increase its height ( $h$  in Fig. 1) so that it can better fit in the experimental system.

The maximum width of the sample in the  $z$ -direction is  $W = 56$  mm and the height in the  $y$ -direction is  $h = 203$  mm. The cylinders were held in place by two wooden pieces with holes carved by a numerical control drill. The dispersion for the radius of cylinders was measured and it was found to be less than 3% of nominal value [25]. The aspect ratio ( $AR$ ) of the sample, defined as  $AR = L/2r$ , was 42. This value was chosen to assure a negligible influence of the finitude in the  $x$ -direction on the measurements, that is attained for  $AR > 10$  (as stated in basic texts of electromagnetism like Bohren and Huffman [27]). We performed the measurements for three cases of shear value ( $\gamma$ ): at 0, 0.1 and 0.2, respectively. These values were selected in order to check and verify the numerical results.

### 2.4. Experimental setup

Transmission spectra of the samples were measured using a vector network analyzer (VNA) HP 8722ES spliced to rectangular horn antennas  $56 \times 44 \times 197$  mm (Narda Model 639), aligned

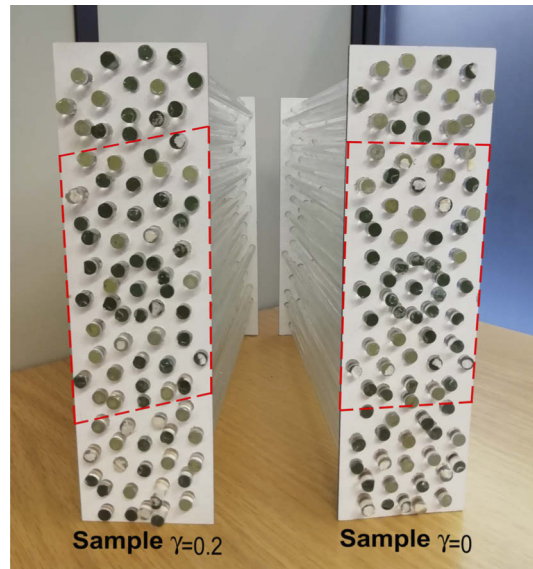


**Fig. 2.** Image of built-up glass sensors with the shear factor applied in the samples. Detail of the fabricated sensor indicating the unit cell used in numerical calculation. The rest of cylinders of the samples are included to match their size to the horn antenna beam.

in  $z$ -direction and separated approximately 200 mm from each other. The sample was placed between both antennas with the cylinders perpendicular to the incidence direction. Transverse magnetic (TM) polarization is considered in this work since antennas show polarization sensitive coupling characteristics, with the electrical field parallel to the short side of its rectangular opening.

All measurements were registered using an incidence electric field vector parallel to the cylinder axes of the sample. The measurement frequency ranges from 9 GHz to 13 GHz. A differential measurement technique is used to register the transmission spectra. First, the transmission spectrum without the sample is recorded on the network analyzer. Next, the transmission spectrum of the sample is measured. The analyzer automatically provides the difference between the spectra with and without the sample. A smoothing algorithm Savitzky-Golay [28] from VNA (span for the moving average of 6 samples) was used to reduce the ripple noise of the measurements. The number of samples in the experimental transmission measurements is 1601 which limits the maximum resolution of the measurements to 2.5 MHz. An outline of the experimental setup can be seen in Fig. 3 [25].

### 2.5. Calculation procedure

Numerical calculations were performed with CST Microwave Studio, a commercial code based on the Finite Integration time-domain Method (FIM) [29]. This program is an electromagnetic field simulation software package especially suited for analysis and design in the high-frequency range.

We employed two solver tools available in CST MW Studio package to simulate the studied structure. First, we use the frequency solver with a tetrahedral adaptive mesh refinement to calculate the transmission spectra considering two dimensional pattern of cylinders but infinite in the  $y$ -direction and assuming infinite length cylinders in the  $x$ -direction. Therefore, the structure is only finite in the incidence direction of the radiation ( $z$ -direction). Second, we used a transient solver with a hexahedral adaptive mesh refinement to calculate the transmission spectra of



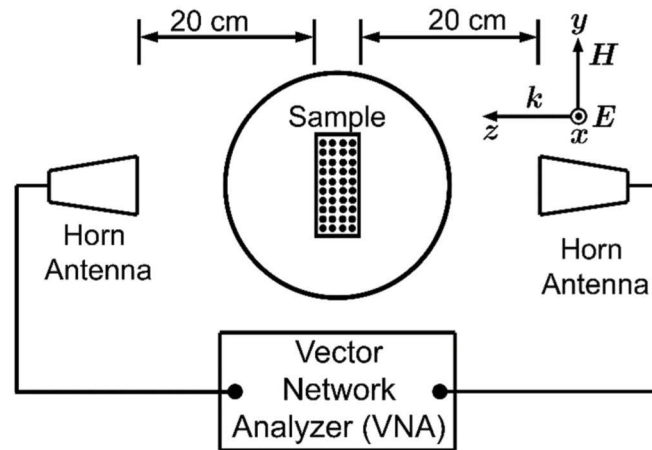


**Fig. 3.** Outline of the experimental setup. The sample is placed at the center and perpendicular to the antennas. The cylinders point at the depicted plane (in the  $x$ -direction), while radiation is emitted and detected perpendicularly ( $z$ -direction) by horn antennas connected to a vector network analyzer (VNA).

the finite sample measured (finite in all directions). Following the specifications of the actual antennas used in the experimental setup, two horn antennas were modeled in CST MW Studio. Besides, two waveguides ports (WR-90) of size  $22.86 \times 10.16$  mm, were coupled to the simulated antennas for the calculations of finite samples measured. Horn antennas were simulated exciting the structure with an electric field polarized along the  $x$ -axis (TM polarization). In all cases (measured and calculated) we keep the separation and the axis definition shown in Fig. 3, where  $z$  is the direction of radiation propagation and  $x$  the cylinder length direction.

### 3. Results and discussion

The relevant variable of the system under study is the frequency position of the states inside the gap in the frequency spectrum and its variation with the sample deformation. There is a state always present in the frequency response of the structure, even when shear is not applied (let's call it S). However, a new resonance arises from shearing the sensor (labeled R). This new state undergoes a variation of its frequency position opposite to the state S. This behavior allows a differential sensing configuration, and we can obtain the magnitude of shear from the frequency shift between both resonances in the bandgap.

The states S and R can be clearly seen in Fig. 4 that shows a color map of the calculated response of the prototype previously described (Fig. 1). Curves were obtained by simulating the transmission spectra of the sensor for different values of shear, and the collection of these curves is presented as a color map. Vertical axis represents the frequency normalized to edge length  $a$  ( $a/\lambda$ ), resulting in a dimensionless parameter as well as in the actual measurement units (GHz) ranging from 9 to 13 GHz. Horizontal axis depicts the shear parameter of the sample (ranging from 0 to 0.3) while transmitted intensity for each case is presented as the color of the points in the figure and varies from -2 to -20 dB (corresponding to 0.8 to 0.1 in linear scale).

In Fig. 4, we see the frequency response of the sensor presenting a remarkable bandgap from 9.5 to 12 GHz. As shear is increased, the bandwidth of the band gap becomes smaller. Also, the abovementioned two states are localized in the gap as inclined straight lines (red and yellow). Both states change their frequency position linearly with the shear value applied. S state (intense red intense in the figure) decreases its frequency value as shear is higher, in contrast, the R state (yellow and blue line) increases its value. The linear evolution shown by the resonances

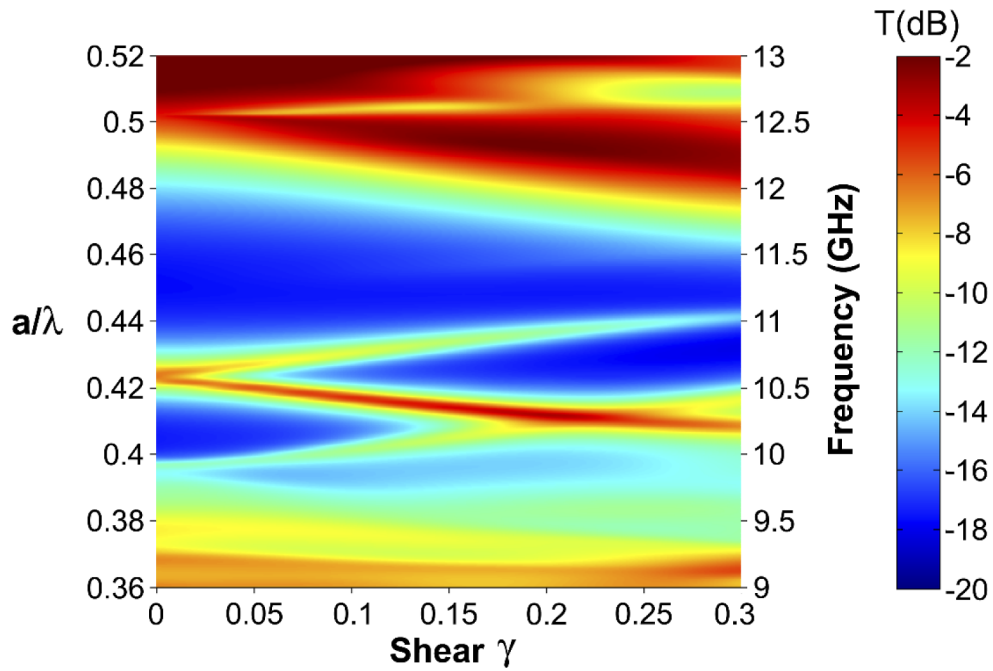


**Fig. 4.** Color map plot of the calculated transmission spectra (dB) as a function of shear parameter ( $\gamma$ ) and frequency. Oblique, descending with the shear, red/yellow line corresponds to sensing state (S) and oblique ascending yellow line to reference state (R).

as the shear is modified makes the structure a good candidate to design a sensing system for deformation.

It is possible to design a differential sensor based on opposite evolution of the resonances inside the gap when strain forces are applied. The evolution of these resonances is shown in Fig. 5(a) while Fig. 5(b) presents their difference. This would be the calibration curve of the prototype sensor. This difference increases the overall sensitivity by adding the 4% upward shift of the S state with the 4% downward of R state. Besides, as is well known, differential operation in sensing systems provides multiple advantages such as systematic error cancellation, cross-sensitivities canceling and noise reduction.

The evolution of the calibration curve up to 0.3 of shear can be considered almost linear with a small error. Hence, we use a linearization in the whole interval. In Fig. 5(b) we find a total frequency shift of 0.81 GHz, corresponding to a total strain variation of 65387  $\mu\epsilon$  (corresponding to a shear variation from 0 to 0.3). Considering a linear variation as previously mentioned, the sensitivity is obtained as the ratio of these two numbers, obtaining a value of as 12.4 kHz/ $\mu\epsilon$ . We have also estimated the linearity error by considering the linear calibration curve [Fig. 5(b)] and we obtain a value smaller than 4%, except for the extreme values where the error reaches 6%. These parameters of sensitivity and linearity extended in a span ranging from 0 to 65387  $\mu\epsilon$  are comparable to those of commercial strain measurement systems. Therefore, the presented prototype has shown the feasibility of the sensing principle we propose.

However, the validation of the sensing principle has been based on calculation data. In order to assure that these results can be trusted, we measured the transmission of physical prototypes of the structures under study as previously described in sub-section 2.3 (Fig. 6). The same geometrical configuration of the measurement (including the antennas) was also modeled in the simulator expecting a better fitting with the corresponding transmission values [26]. It is important to note

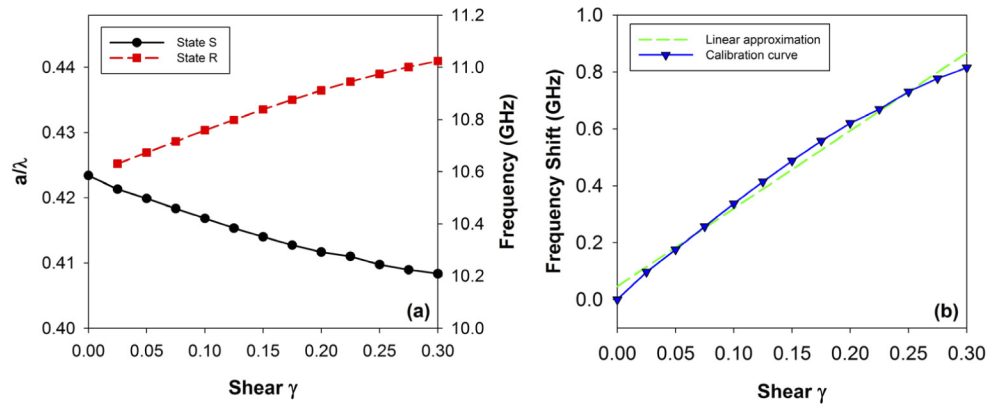


**Fig. 5.** (a) Peaks in frequency response and (b) differential peak in frequency as a function of the applied shear, this is the calibration curve of the sensor including its linear approximation (green dashed line).

the different calculation procedure in the case of the infinite sample sensor (where plane wave excites an infinite structure in two directions of the space,  $x$  and  $y$ ) and in the case of transmission measurements (where a totally finite sample is illuminated by finite antennas). The results of these measurements and as well as the calculations are presented in Fig. 7. The figure shows the transmission spectra (transmittance versus frequency) for three different values of shear,  $\gamma$  of 0, 0.1 and 0.2, respectively. As it can be seen, the agreement between calculation and measurements is very good. The two peaks are found at the same frequency and present the same evolution with shear (movement in opposite direction) both experimental and calculated. It is important to note that the agreement between measurement and finite calculations is significant, the general outline of the curves is similar, with good coincidence in the transmittance values shown. Small discrepancies in the edge of band gap could be due to an angular error of antennas alignment and the fact that the sample is much smaller than the illuminated area of the antennas. The theoretical Q-factor value of states R and S has been calculated for the fabricated prototypes, presenting an average value of 120 and 100, respectively. The experimental Q-factor of the resonances is slightly lower than calculated due to the experimental error, with an average value of 60 and 30 for the resonances R and S, respectively. The Q-factor obtained in the device could be improved by increasing the refractive index of the cylinders.

We have analyzed and characterized a PhC device arisen from Penrose quasi-crystals in the microwave range, however, the obtained results can be directly extrapolated to other ranges since electromagnetism has no fundamental length that determines the response. Our model has been implemented in macroscopic scale but this is not a limitation since it could be also made and tested in the optic regime if the dielectric permittivity in both scales remains constant. Materials with real dielectric permittivity similar to soda-lime glass and with small losses are commonly used in optic range. Some examples of these materials are Alumina, Silicon Carbide, Zirconia, Silicon Nitride, or Titania. However, the best candidate to reproduce the results presented in this paper is Titania since it presents a refractive index of 2.06, close to the value used in the macroscopic sample ( $n=2.12$ ) [30]. Besides, Titania is loss-free in the optical range from 1 to  $1.5 \mu\text{m}$  with small dispersion, reproducing almost exactly the conditions employed in the design for the microwave range. Thus, we have calculated the performance of the sensing system in the optical range using Titania cylinders. The geometrical parameters used to design in the microwave range have been resized by a scale factor of 24000. The optical response of sensing resonances R and S resonances now varies between 1200 and 1110 nm. The sensitivity of the resulting optical



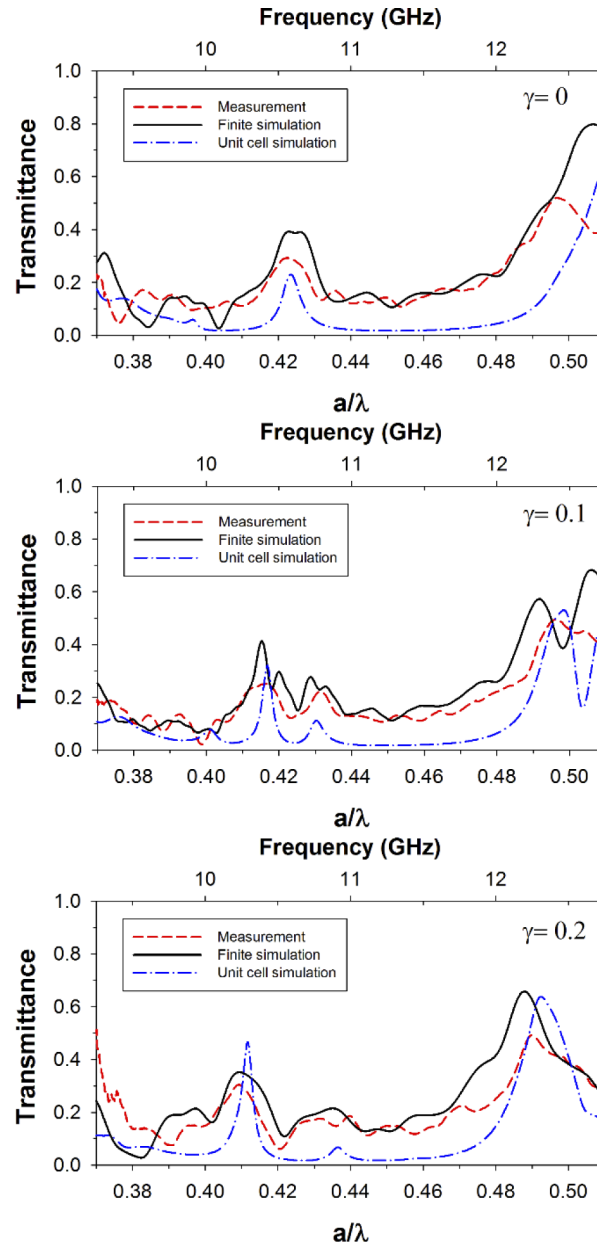


**Fig. 6.** Calculated (black solid and blue dot-dashed lines) and measured (red dashed line) transmission spectra for the fabricated prototypes as a function of normalized frequency ( $a/\lambda$ ).

system is 1.3 nm/ $\mu\epsilon$  which does not mean a technological problem of measurement resolution for the actual optical instrumentation.

#### 4. Conclusions

We have designed and fabricated a differential strain sensor prototype based on quasicrystal-like structure of dielectric cylinders that contains a decagonal ring resonator. The sensor generates a stop band where two modes are excited when an external strain force is applied. Both modes vary their frequency value, as strain is increased: the reference mode (R mode) shifts to smaller frequency values whereas the sensing mode (S mode) shifts to higher frequency values. The strain is proportional to the frequency difference between both modes.

Transmission spectra for two samples with different strain applied were experimentally obtained in microwave range by using soda-lime glass cylinders of permittivity  $\epsilon_r=4.5$  and radius 3 mm. The sensor shows a linear dependence with the strain as well as a sensitivity of 0.012 MHz/ $\mu\epsilon$  for a strain range from 0 to 65387  $\mu\epsilon$ . We found that the linearity error of the samples is lower than 4%. The agreement between measurements and simulations is good, which makes these structures excellent candidates to design differential strain sensors in the optical range made with Titania and presenting a sensitivity of 1.3 nm/ $\mu\epsilon$ .

**Funding.** Ministerio de Ciencia, Innovación y Universidades (RTI2018-094475-B-I00).

**Acknowledgments.** The authors gratefully acknowledge Santiago de Miguel and David Llorente for their technical support.

**Disclosures.** The authors declare that there are no conflicts of interest related to this article.

#### References

1. S. John, "Strong localization of photons in certain disordered dielectric superlattices," *Phys. Rev. Lett.* **58**(23), 2486–2489 (1987).
2. E. Yablonovitch, "Inhibited Spontaneous Emission in Solid-State Physics and Electronics," *Phys. Rev. Lett.* **58**(20), 2059–2062 (1987).
3. B. Dong, J. Hao, C. Liaw, B. Lin, and S. C. Tjin, "Simultaneous strain and temperature measurement using a compact photonic crystal fiber inter-modal interferometer and a fiber Bragg grating," *Appl. Opt.* **49**(32), 6232–6235 (2010).
4. Y. Wang, H. Bartelt, W. Ecke, R. Willsch, J. Kobelke, M. Kautz, S. Brueckner, and M. Rothhardt, "Sensing properties of fiber Bragg gratings in small-core Ge-doped photonic crystal fibers," *Opt. Commun.* **282**(6), 1129–1134 (2009).
5. Y.-P. Wang, L. Xiao, D. N. Wang, and W. Jin, "Highly sensitive long-period fiber-grating strain sensor with low temperature sensitivity," *Opt. Lett.* **31**(23), 3414–3416 (2006).
6. W. Shin, Y. L. Lee, T. J. Eom, B.-A. Yu, and Y.-C. Noh, "Temperature insensitive strain sensor based on long period fiber grating pair in photonic crystal fibers," in *2009 14th OptoElectronics and Communications Conference (IEEE, 2009)*, pp. 1–2.
7. H. K. Baghbadorani and J. Barvestani, "Effect of Uniaxial Strain on the Performance of One-Dimensional Graphene Fibonacci Photonic Crystal Biosensors," *J. Lightwave Technol.* **36**(23), 5406–5412 (2018).
8. T.-W. Lu, C.-C. Wu, and P.-T. Lee, "1D photonic crystal strain sensors," *ACS Photonics* **5**(7), 2767–2772 (2018).
9. Y. Zhang, Y. Zhao, and R. Lv, "A review for optical sensors based on photonic crystal cavities," *Sens. Actuators, A* **233**, 374–389 (2015).
10. B. T. Tung, D. V. Dao, T. Ikeda, Y. Kanamori, K. Hane, and S. Sugiyama, "Investigation of strain sensing effect in modified single-defect photonic crystal nanocavity," *Opt. Express* **19**(9), 8821–8829 (2011).
11. Bui Thanh Tung, Dzung Viet Dao, S. Susumu, Hoang Minh Nguyen, S. Rogge, and H. W. M. Salemink, "Strain sensitivity of a modified single-defect photonic crystal nanocavity for mechanical sensing," in *2010 IEEE Sensors (IEEE, 2010)*, pp. 2585–2588.
12. T. Stomeo, M. Grande, A. Qualtieri, A. Passaseo, A. Salhi, M. De Vittorio, D. Biallo, A. D'orazio, M. De Sario, V. Marrocco, V. Petruzzelli, and F. Prudeniano, "Fabrication of force sensors based on two-dimensional photonic crystal technology," *Microelectron. Eng.* **84**(5-8), 1450–1453 (2007).
13. D. Yang, H. Tian, and Y. Ji, "Microdisplacement sensor based on high-Q nanocavity in slot photonic crystal," *Opt. Eng.* **50**(5), 054402 (2011).
14. T. T. Mai, F.-L. Hsiao, C. Lee, W. Xiang, C.-C. Chen, and W. K. Choi, "Optimization and comparison of photonic crystal resonators for silicon microcantilever sensors," *Sens. Actuators, A* **165**(1), 16–25 (2011).
15. B. Li and C. Lee, "NEMS diaphragm sensors integrated with triple-nano-ring resonator," *Sens. Actuators, A* **172**(1), 61–68 (2011).

16. T. Sreenivasulu, B. T. Rao, G. Hegde, and S. T., "Photonic crystal ring resonator based force sensor: Design and analysis," *Optik* **155**, 111–120 (2018).
17. C. Lee, R. Radhakrishnan, C.-C. Chen, J. Li, J. Thillaigovindan, and N. Balasubramanian, "Design and Modeling of a Nanomechanical Sensor Using Silicon Photonic Crystals," *J. Lightwave Technol.* **26**(7), 839–846 (2008).
18. Y. Yang, F. Yang, H. Wang, W. Yang, and W. Jin, "Temperature-insensitive hydrogen sensor with polarization-maintaining photonic crystal fiber-based Sagnac interferometer," *J. Lightwave Technol.* **33**(12), 2566–2571 (2015).
19. L. M. Hu, C. C. Chan, X. Y. Dong, Y. P. Wang, P. Zu, W. C. Wong, W. W. Qian, and T. Li, "Photonic Crystal Fiber Strain Sensor Based on Modified Mach–Zehnder Interferometer," *IEEE Photonics J.* **4**(1), 114–118 (2012).
20. S. Wang, P. Lu, L. Mao, D. Liu, and S. Jiang, "Cascaded interferometers structure based on dual-pass Mach–Zehnder interferometer and Sagnac interferometer for dual-parameter sensing," *Opt. Express* **23**(2), 674–680 (2015).
21. L. M. Fortes, M. C. Gonçalves, and R. M. Almeida, "Flexible photonic crystals for strain sensing," *Opt. Mater.* **33**(3), 408–412 (2011).
22. C. G. Schäfer, M. Gallei, J. T. Zahn, J. Engelhardt, G. P. Hellmann, and M. Rehahn, "Reversible Light-, Thermo-, and Mechano-Responsive Elastomeric Polymer Opal Films," *Chem. Mater.* **25**(11), 2309–2318 (2013).
23. O. L. J. Pursiainen, J. J. Baumberg, K. Ryan, J. Bauer, H. Winkler, B. Viel, and T. Ruhl, "Compact strain-sensitive flexible photonic crystals for sensors," *Appl. Phys. Lett.* **87**(10), 101902 (2005).
24. K. Wang, "Light localization in photonic band gaps of quasiperiodic dielectric structures," *Phys. Rev. B* **82**(4), 045119 (2010).
25. Á. Andueza, J. Pérez-Conde, and J. Sevilla, "Strong angular dependence of resonant states in 2D dielectric cylinder rings," *J. Appl. Phys.* **124**(17), 174903 (2018).
26. Á. Andueza, K. Wang, J. Pérez-Conde, and J. Sevilla, "Optimal width of quasicrystalline slabs of dielectric cylinders to microwave radiation transmission contrast," *J. Appl. Phys.* **120**(8), 083101 (2016).
27. C. F. Bohren and D. R. Huffman, *Absorption and Scattering of Light by Small Particles* (Wiley, 1983).
28. A. Savitzky and M. J. E. Golay, "Smoothing and Differentiation of Data by Simplified Least Squares Procedures," *Anal. Chem.* **36**, 1627–1639 (1964).
29. M. Clemens and T. Weil, "Discrete Electromagnetism with the Finite Integration Technique," *Prog. Electromagn. Res.* **32**, 65–87 (2001).
30. S. Sarkar, V. Gupta, M. Kumar, J. Schubert, P. T. Probst, J. Joseph, and T. A. F. König, "Hybridized Guided-Mode Resonances via Colloidal Plasmonic Self-Assembled Grating," *ACS Appl. Mater. Interfaces* **11**(14), 13752–13760 (2019).